Very fast simulation of growth competition between columnar dendritic grains during melt pool solidification

Quentin Dollé, Daniel Weisz-Patrault

▶ **To cite this version:**

Quentin Dollé, Daniel Weisz-Patrault. Very fast simulation of growth competition between columnar dendritic grains during melt pool solidification. Computational Materials Science, 2024, 243, pp.113112. 10.1016/j.commatsci.2024.113112 . hal-04608258

HAL Id: hal-04608258
https://hal.science/hal-04608258

Submitted on 11 Jun 2024

HAL is a multi-disciplinary open access archive for the deposit and dissemination of scientific research documents, whether they are published or not. The documents may come from teaching and research institutions in France or abroad, or from public or private research centers.

L'archive ouverte pluridisciplinaire **HAL**, est destinée au dépôt et à la diffusion de documents scientifiques de niveau recherche, publiés ou non, émanant des établissements d'enseignement et de recherche français ou étrangers, des laboratoires publics ou privés.

Very fast simulation of growth competition between columnar dendritic grains during melt pool solidification.

Quentin Dollé[a,b], Daniel Weisz-Patrault[a,*]

[a]*LMS, CNRS, École Polytechnique, Institut Polytechnique de Paris, F-91128 Palaiseau, France*
[b]*Univ. Lille, CNRS, Centrale Lille, UMR 9013 - LAMCUBE - Laboratoire de Mécanique, Multiphysique, Multi-échelle, F-59000 Lille, France*

Abstract

This paper presents a very fast numerical approach to simulate microstructures resulting from melt pool solidification including growth competition of columnar dendritic grains, and equiaxed grains nucleated from the melt. To reduce computation time, the key contribution is the development of an upscaling strategy, which instead of considering each dendrite individually consists in defining an average solidification front based on physically-informed dendritic growth velocity. The proposed approach also relies on dendritic preferred growth direction, and favorably oriented grain criterion to determine which grain survives the competition. To significantly reduce the total number of degrees of freedom *Voronoi tessellations* are used instead of regular grids for numerical implementation. Indeed, 3D regular grids typically leads to N^3 degrees of freedom while *Voronoi tessellations* lead to only $3N$, which dramatically reduces computation cost. This work is therefore a high-throughput approach enabling large data set generation to explore statistical features of microstructures with respect to melt pool properties. Results have been compared to experimental data, and to phase field and cellular automaton simulations in 2D only. Simulated microstructures are similar as those obtained with cellular automaton. Comparisons in 3D are left for future work. In addition, a convergence analysis is provided for 3D simulations, with thermal conditions corresponding to metal additive manufacturing to demonstrate how the present work can be used in practice.

Keywords: Solidification, Microstructure, Numerical metallurgy, Growth competition

1. Introduction

Several major fabrication processes rely on melt pool solidification. Simulation tools have been extensively developed to predict the final grain structure and crystal orientations given cooling conditions [1]. Indeed, microstructures formed during solidification are of particular interest as material properties (e.g., the hardening law) significantly depend on crystallographic and morphological textures. In most processes involving melt pool solidification such as welding or additive manufacturing processes, dendritic columnar and dendritic equiaxed grains are generated [2].

*Corresponding author: *daniel.weisz-patrault@cnrs.fr*

On the one hand, columnar grains are formed through epitaxial growth directly from the grains surrounding the liquid metal and inherit their crystal orientation. The resulting crystallographic texture is therefore mostly influenced by competitive dendritic growth mechanisms, which combine the local thermal gradient direction and the preferred growth direction (e.g., one of the six $\langle 001 \rangle$ directions in face cubic centered (FCC) or body centered cubic (BCC) alloys). On the other hand, equiaxed grains can nucleate from randomly distributed impurities in the liquid phase and undergo equiaxed dendritic growth. Therefore, one of the major concept to characterize the typology of microstructures formed during solidification is the columnar to equiaxed transition (CET) to determine in which regions of the microstructure the grains are equiaxed or columnar. CET mostly depends on the temperature gradient denoted by G (K.m^{-1}) and the solidification front velocity denoted by V (m.s^{-1}). Morphological ratios G/V (K.s) or G^2/V (K^2.s.m^{-1}) [3] have been established to determine whether the solidification mode is columnar dendritic or equiaxed dendritic (or even planar and cellular but such regimes are usually not reached for rapid solidification). Moreover, the cooling rate at the solidification front is strongly correlated with the average size of equiaxed grains [2].

Such a general description though does enable to predict detailed microstructures resulting from rapid solidification. Therefore, several classical approaches have been developed to simulate dendritic growth. At the scale of dendrites, level-set functions have been used to capture the sharp liquid-solid interface and are updated by solving the Stefan equation [4]. Phase field (PF) models enable to track the solid-liquid interface introducing a continuous variable, which corresponds to continuous transition between phases. One advantage of PF approaches is to avoid specifying boundary conditions at moving interfaces [1, 5], as the phase field variable is governed by volume equations such as heat and solute transport equations [6]. Level-set and PF methods are well-established as references for quantitative modeling of dendritic growth [4, 7] and their simulations have greatly deepened our knowledge on the directional solidification [8].

One of the main drawback of such simulations is their computation cost associated to the very fine scale at which the liquid to solid phase transition is considered (i.e., dendritic arms growth). Alternative approaches have therefore been developed at slightly larger scales to reduce computation time. Instead of considering dendrites individually by detailing the liquid-solid interface, dendritic needle network (DNN) approaches have been developed to reduce the size of the problem by considering dendritic primary, secondary and higher order branches as a network of sharp needles interacting through the solutal diffusion field [9, 10]. The tip velocity of each needle is determined by combining solvability and solutal flux balance conditions involving contour integral methods. This physically-based multiscale model has been used to simulate dendritic growth during solidification, and was in good agreement with PF simulations while being significantly faster. In addition, the columnar grain growth and CET have also been determined in 2D [11] and in 3D [12].

Furthermore, one of the most popular numerical method to simulate the formation of microstructure during solidification is cellular automaton (CA), consisting in a regular grid of cells to which an index corresponding to the state of the cell is assigned (i.e., crystal orientation or liquid) [13]. A set of physically-informed rules enables to modify the cells state and thus to simulate the system evolution. In addition, thermal finite element analysis (FEA) is usually coupled to CA into a multi-scale model called cellular automaton finite element (CAFE) to compute both temperature

kinetics (i.e., cooling rates and temperature gradients) and the forming grain structure [13]. The advantage of coupling CA and FEA lies in the fact that FEA enables to solve heat conduction, fluid convection and solute diffusion [1], and can be used as inputs in the CA simulation. To spare computation time, the mesh used in the FEA is usually coarser than the grid used in the CA as the scale of dendritic growth is finer than typical length scales of temperature diffusion. Thermal quantities are then interpolated onto the cells of the CA grid. The undercooling (i.e., the difference between the liquidus temperature and the actual temperature) is therefore determined for the cells belonging to the liquid-solid interface and their neighbors, which in turn enables to determine the growth rate of dendrites along their preferential growth direction. In addition, nucleation is also considered in the liquid if undercooling exceeds a critical threshold. The corresponding liquid cells are thus switched to solid cells with random crystal orientation [13, 14]. For instance, CAFE models have also been used within the context of additive manufacturing [15, 16].

Of course, comprehensive numerical approaches to simulate solidification (e.g., level-set, PF, DNN and CAFE) depend on conditions such as the detailed grain structure from which epitaxial dendritic growth takes place, which depends on (i) surrounding grains with unknown crystal orientations, and (ii) the random crystal orientations of dendritic equiaxed grains nucleated from impurities randomly distributed in the melt. In practice, this detailed information is unknown, and can only be modeled using random variables [17]. Therefore despite the accuracy of physically-based models, the exact grain structure resulting from the fabrication process cannot be obtained. Numerical simulations should be seen as draws of random variables representing the formation of microstructures during the solidification process. The main difficulty with comprehensive numerical methods is their computational cost which makes difficult to statistically explore the solidification problem by computing a large number of draws (i.e., different possible microstructures) in the entire solidified structure although some works already performed such a statistical treatment using fast CA approaches [15, 18].

To overcome this difficulty, this contribution aims at developing a very fast numerical approach including growth competition of columnar dendritic grains, and equiaxed grains nucleated from the melt. The proposed upscaling strategy to reduce computation time is similar to the one developed for grain growth during annealing in [19–21]. It relies on the development of an algorithm based on 1) solidification maps to determine the region where CET occurs [3], 2) the dendritic preferred growth direction, 3) the application of the Walton and Chalmers criterion [22] relying on the concept of *favorably oriented grain* (FOG) to determine which grain survives the competition [8, 23–25], and 4) a solidification front propagation rule along the thermal gradient direction. To significantly reduce the total number of degrees of freedom (DoF), *Voronoi tessellations* are used to implement the formation of the microstructure instead of fine regular grids as in CA. For each temperature field history, the proposed model enables to carry out a large number of simulations in order to characterize probability density functions of various distributions such as grain size, grain shape, crystal orientation, crystal disorientation between neighbouring grains etc. It should be noted that PF simulations of grain boundaries (GB) during competitive growth are not necessarily in good agreement with a strict application of the FOG criterion [8, 23], however it is still used in recent models aiming at reducing computational cost [26] for larger scale domains. Thus, Pineau et al. [7] proposed alternative competitive growth criteria in 2D focusing on GBs directions so that the competition is implicit (i.e., grains stop growing when their GBs are converging), whereas the

FOG criterion explicitly defines which grains survive the competition. These alternative criteria are derived as phenomenological laws fitted on PF simulations. Since Voronoi tessellations do not enable to control GBs, these phenomenological criteria cannot be implemented easily by following the present strategy.

Of course, the present fast numerical approach does not aim at capturing the behavior of each individual dendrite with high accuracy. In addition, the precise plane orientations of GBs for pairs of converging and diverging grains is usually used as an important benchmark for solidification models, but the present strategy does not aim at capturing this aspect either. Indeed, we rather focus on large aggregates for which the precise plane orientations of GBs of individual grains are not of particular interest. We attempt to capture the grain structure with correct size, average shape and crystal orientations so that the statistical properties of the grain structure at larger scale are determined within short computation time. The proposed method is therefore aimed to be sufficiently fast to carry out parametric studies, optimizations or construct large databases to feed machine learning algorithms.

The paper is organized as follows. The model is detailed in section 2, and consists in determining the columnar and equiaxed regions, the grain size of equiaxed grains, and the competitive growth based on Voronoi tessellation techniques. In section 3, the model is compared to classical experimental data, and to CA and PF simulations in 2D only in order to test the ability to accurately capture the microstructures arising during melt pool solidification. Comparison in 3D are left for future work. In addition a convergence analysis is provided in 3D. Conclusive remarks are given in section 4.

2. Methods

Temperature T (K), solutes concentrations c_j (vol%) (where j is the index of the alloying elements) and solid/liquid (S/L) interface curvature κ (m^{-1}) affect the bulk and surface energies, which leads to define driving forces associated to thermal and solute content as well as the interface curvature. These driving forces are usually reduced into the concept of undercooling ΔT, which characterizes the difference between the liquidus temperature $T_{\mathrm{liq}}(c_j, \kappa)$ at which the phase transition would occur at equilibrium, and the actual temperature T so that:

$$\Delta T(\boldsymbol{x}, t) = T_{\mathrm{liq}}(c_j(\boldsymbol{x}), \kappa(\boldsymbol{x})) - T(\boldsymbol{x}, t) \tag{1}$$

Where t is the time, and $\boldsymbol{x}$ is a position. Thermal, solutal and curvature undercooling are therefore usually defined to account for the different contributions of the driving forces. A power law is usually fitted to express the local solidification front normal velocity V as a function of the undercooling:

$$V(\boldsymbol{x}, t) = \alpha\, \Delta T(\boldsymbol{x}, t)^{\beta} \tag{2}$$

Where α and β are material parameters. The solubility of alloying elements is not identical in liquid and solid phases. As a result, as shown in figure 1 near the S/L interface the solute content deviates from the nominal composition denoted by $\overline{c}_j$ obtained from the chemical composition of the studied material. The distribution of solute content at the S/L interface along with local

curvatures are responsible for heterogeneous distribution of undercooling. Then, according to (2) the evolution of the solidification front is heterogeneous, and results in complex dendritic patterns.

Since very short computation time is aimed, an averaging process is proposed to summarize the effects of different physical mechanisms arising at fine scale into easily manageable evolution laws. First, there is a strong coupling between solidification and heat conduction because of the latent heat of fusion. Nevertheless, even though liquid to solid phase transition arises at the S/L interface (i.e., along the dendrite boundary) one can smooth the effect of the latent heat of fusion by assuming that it only depends on the phase fraction rate, which represents in average the evolution of dendrites. Therefore, the first assumption is to compute the temperature field with latent heat of fusion before determining the solidification front regardless of the detailed dendritic structure instead of a fully coupled problem.

In addition, it should be noted that at the large scale where dendrites are not distinguished, the state of matter can be either *liquid*, *solid* or *mushy* (i.e., in a liquid+solid mixture where dendrites are surrounded by the liquid phase), while only liquid and solid phases exist at the fine scale of individual dendrites (see. figure 1a). To avoid long computation time, the larger scale is considered, and therefore an average solidification front (ASF) is considered instead of the detailed S/L interface. At each time t, the ASF is defined as an isotherm whose temperature denoted by $T_{\text{ASF}}(t)$ is to be determined such as the normal velocity of the ASF matches in average the definition of the dendritic velocity (2). It should be noted that the undercooling arising in (2) involves computing T_{liq}, which explicitly depends on local solute content c_j and curvature κ. (i) Diffusion mechanisms are assumed to be confined near the S/L interface, and mass conservation enables to consider that the average solute content over the mushy zone is close to the nominal solute content $\bar{c}_j$, see. figure 1b. Therefore the undercooling in (2) is computed using $\bar{c}_j$ instead of the detailed solute content c_j. (ii) In addition, the curvature of the S/L interface is a succession of positive, zero and negative curvatures following the dendritic arms, and roughly averages to the curvature of the T_{ASF}-isotherm, which is negligible in comparison to local curvatures involved at the dendrite tips. Therefore the undercooling in (2) is computed using $\kappa = 0$.

Furthermore, the normal velocity of the ASF is obtained from the known temperature field history $T(\boldsymbol{x}, t)$ as follows:

$$\forall \boldsymbol{x} \in \Gamma_t(T_{\text{ASF}}(t)),\ V_{\text{ASF}}(\boldsymbol{x}, t) = \frac{\dot{T}(\boldsymbol{x}, t)}{G(\boldsymbol{x}, t)} \tag{3}$$

Where the temperature gradient reads $G(\boldsymbol{x}, t) = \|\boldsymbol{\nabla} T(\boldsymbol{x}, t)\|$, and where $\Gamma_t(T_0)$ is the T_0-isotherm surface defined as follows:

$$\Gamma_t : T_0 \in \mathbb{R}^+ \mapsto \{\boldsymbol{x},\ T(\boldsymbol{x}, t) = T_0\} \subset \mathbb{R}^3 \tag{4}$$

Hence by considering that the normal velocity of the ASF should fit in average the definition of the dendritic velocity (2), the ASF temperature reads:

$$T_{\text{ASF}}(t) = T_{\text{liq}} - \left(\frac{\overline{V}_{\text{ASF}}(t)}{\alpha}\right)^{\frac{1}{\beta}} \tag{5}$$

Where T_{liq} is computed for known nominal solute contents $\overline{c}_j$ and zero curvature $\kappa = 0$, and where $\overline{V}_{\text{ASF}}(t)$ is the average normal velocity of the ASF, which reads:

$$\overline{V}_{\text{ASF}}(t) = \frac{1}{|\Gamma_t(T_{\text{ASF}}(t))|} \int_{\Gamma_t(T_{\text{ASF}}(t))} V_{\text{ASF}}(\boldsymbol{x}, t)\, \mathrm{d}S \tag{6}$$

where $|\Gamma_t(T_{\text{ASF}}(t))|$ is the isotherm surface (in 3D) or length (in 2D). Knowing the temperature field history $T(\boldsymbol{x}, t)$, the ASF temperature $T_{\text{ASF}}(t)$ is therefore determined by solving (5), which leads to identify $\Gamma_t(T_{\text{ASF}}(t))$ as a function of time. To do so a simple and fixed-point iterative procedure consists in setting an initial trial temperature $T_{\text{ASF}}(t)$ and repeating the 3 following steps until convergence:(i) compute the corresponding velocity $V_{\text{ASF}}(\boldsymbol{x}, t)$ using (3), (ii) compute the corresponding average $\overline{V}_{\text{ASF}}(t)$ using (6), and (iii) compute a new evaluation of $T_{\text{ASF}}(t)$ using (5). In addition, T_{ASF} is bounded between T_{sol} and T_{liq} to be consistent with the very definition of the ASF.

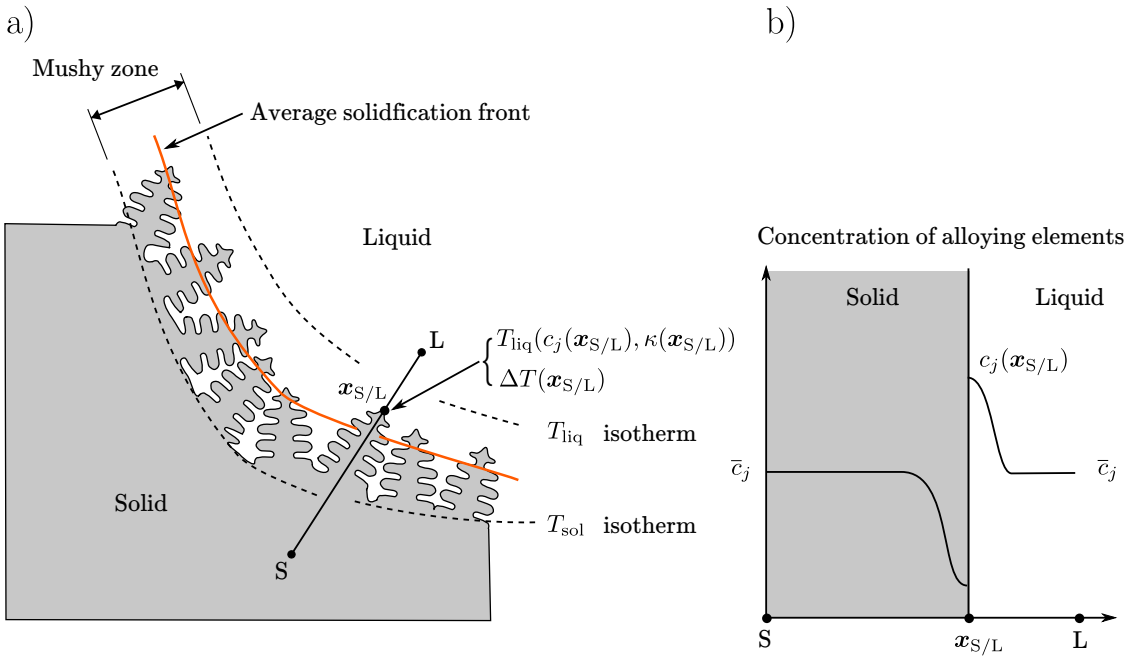

Figure 1: a) schematic view of the detailed solidification front and the average solidification front defined as the T_{ASF}-isotherm, and b) schematic view of diffusion of alloying elements near dendrite tips.

In addition to the definition of the ASF, simple tools are also used to upscale solidification mechanisms: 1) solidification maps, 2) a geometrical relationship between dendritic and solidification front velocity, 3) a geometrical criterion of grain selection in the competitive growth, and 4) a construction rule of Voronoi tessellations.

1) *Solidification maps*. To avoid fine scale computations, solidification maps are used to simply summarize the relevant physical phenomena governing CET. Solidification maps have been established for various alloys on the basis of experimental observations to characterize CET as a function of thermal gradient and solidification front velocity [3, 27] (see. figure 2). Thus,

solidification maps are used in this contribution to determine columnar and equiaxed regions by extracting from the temperature field history the temperature gradient $G(\boldsymbol{x})$ and the ASF velocity $V_{\text{ASF}}(\boldsymbol{x})$ as defined in (3) (with $\boldsymbol{x} \in \Gamma_t(T_{\text{ASF}})$). In the region where equiaxed grains take place, seeds are randomly distributed with random crystal orientations. The average distance

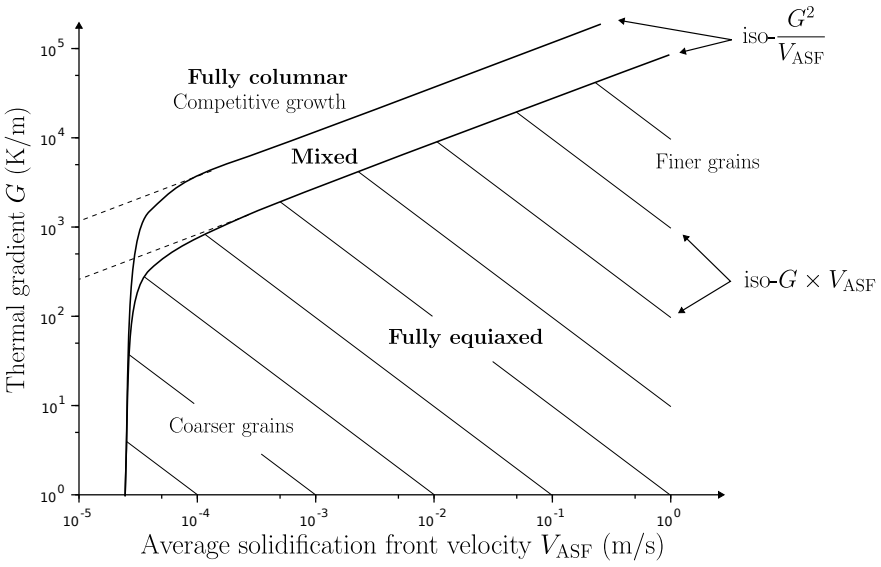

Figure 2: Solidification map for Inconel 718 extracted from [3].

between seeds is determined using the grain size of equiaxed grains, which depends on cooling rates denoted by $\dot{T}(\boldsymbol{x})$ (K.s^{-1}) (with $\boldsymbol{x} \in \Gamma_t(T_{\text{ASF}})$). In the literature, several approaches have been used to assess grain size in melt pool solidification [28]. In this paper a simpler empirical approach [29, 30] is chosen to directly relate the grain size d (µm) and the cooling rate at the solidification front in the form of a power law:

$$d = d_0 \times \left(\frac{\chi}{G \times V_{\text{ASF}}} \right)^{\gamma} \tag{7}$$

Where d_0 (µm) is a reference grain diameter arbitrarily set to 1 µm, χ (K.s^{-1}) is an adjustable reference cooling rate, and γ is an adjustable dimensionless coefficient.

2) *Geometrical relationship between dendritic and average solidification front velocity*. Solidification maps only provide for qualitative morphological information, and should be complemented to capture dendritic competitive growth. To avoid fine scale computation of surface and bulk energies to simulate the dendritic growth in details, physical phenomena are summarized into the following simple geometrical growth criterion. Each grain is composed of a family of dendrites sharing the same crystal orientation, and preferential growth direction denoted by $\boldsymbol{d}_{\text{dent}}$ (e.g., $\langle 001 \rangle$ for FCC and BCC). Each dendrite family is growing at a speed denoted by V_{dent}. In melt pool solidification though, it is commonly observed and admitted that grain growth direction denoted by $\boldsymbol{d}_{\text{grain}}$ aligns with the thermal gradient direction denoted by $\boldsymbol{n}$ (i.e., $\boldsymbol{d}_{\text{grain}} = \boldsymbol{n} \propto \boldsymbol{\nabla} T$) instead of $\boldsymbol{d}_{\text{dent}}$ [2, 31]. (By definition of isotherms, $\boldsymbol{n}$ identifies as the

outer normal vector of the T_{ASF}-isotherm.) More generally though, as suggested in [32] and depending on cooling conditions, one can consider that :

$$\boldsymbol{d}_{\mathrm{grain}} = \lambda\, \boldsymbol{n} + (1-\lambda)\, \boldsymbol{d}_{\mathrm{dent}} \tag{8}$$

Where $0 < \lambda < 1$. For the sake of simplicity $\lambda = 1$ in section 3. Therefore, considering that the evolution of the dendrites is constrained by the ASF velocity, one obtains:

$$\forall \boldsymbol{x} \in \Gamma_t(T_{\mathrm{ASF}}),\ V_{\mathrm{ASF}}(\boldsymbol{x}) = V_{\mathrm{dent}}(\boldsymbol{x}) \cos(\varphi(\boldsymbol{x})) \tag{9}$$

Where φ is defined as in figure 3 and reads:

$$\forall \boldsymbol{x} \in \Gamma_t(T_{\mathrm{ASF}}),\ \varphi(\boldsymbol{x}) = \arccos\left(\boldsymbol{d}_{\mathrm{dent}}(\boldsymbol{x}).\boldsymbol{d}_{\mathrm{grain}}(\boldsymbol{x})\right) \tag{10}$$

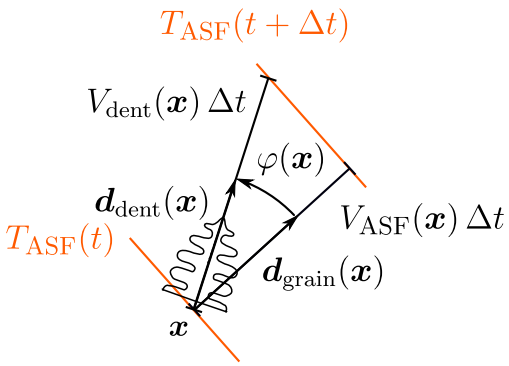

Figure 3: Schematic view of dendritic growth rate.

3) *Geometrical criterion of grain selection in the competitive growth.* The pioneer work of Walton and Chalmers [33] suggests that the grains for which the preferred growth direction and the local thermal gradient direction are best aligned evolve at smaller undercooling (i.e., the dissipated power is smaller for favorably oriented grains), and are more likely to survive. On this basis, the most *favorably oriented grain* (FOG) criteria is used and enables to determine which grain overgrows the other when directions of families of dendrites intersect.
More precisely, each family of dendrites (i.e., all dendrites sharing a common crystal orientation and forming a grain) are modeled as a single straight line propagating along the preferred growth direction $\boldsymbol{d}_{\mathrm{dent}}$. The competitive growth involves considering intersections between pairs of dendrites families with angles φ_1 and φ_2 as defined in (10), and selecting the dendrite which overgrows the other as the one having the smallest angle (i.e., FOG criterion). However, if the intersection between nonparallel straight lines is unequivocally defined in 2D, in general nonparallel straight lines do not intersect in 3D. The intersection is then replaced by the notion of *conflict*, which is defined as in figure 4 by $\delta \leq \delta_0$ where δ is the smallest distance between the two straight lines and $\delta_0 > 0$ an adjustable threshold. Consider two straight lines denoted by $\mathcal{D}_u$ and $\mathcal{D}_v$ defined by the unit vectors $\boldsymbol{u}, \boldsymbol{v}$ (such as $\|\boldsymbol{u}\| = \|\boldsymbol{v}\| = 1$):

$$\begin{aligned} \mathcal{D}_u &= \{\boldsymbol{u}\, t + \boldsymbol{x}_u \in \mathbb{R}^3,\ t \in \mathbb{R}\} \\ \mathcal{D}_v &= \{\boldsymbol{v}\, t + \boldsymbol{x}_v \in \mathbb{R}^3,\ t \in \mathbb{R}\} \end{aligned} \tag{11}$$

The minimum distance δ and the corresponding positions on $\mathcal{D}_u$ and $\mathcal{D}_v$ are defined as follows. Consider the straight line $\mathcal{D}_w$ perpendicular to both $\mathcal{D}_u$ and $\mathcal{D}_v$ defined by:

$$\mathcal{D}_w = \left\{ \boldsymbol{w}\, t + \boldsymbol{x}_w \in \mathbb{R}^3,\, t \in \mathbb{R} \right\} \tag{12}$$

Where $\boldsymbol{w} = \boldsymbol{u} \wedge \boldsymbol{v}$ and $\boldsymbol{x}_w$ is to be determined. The straight line $\mathcal{D}_w$ should intersect both $\mathcal{D}_u$ and $\mathcal{D}_v$ so that there exists $(t_u, t_v, t_w) \in \mathbb{R}^3$ such as:

$$\begin{aligned} \boldsymbol{x}_w &= \boldsymbol{u}\, t_u + \boldsymbol{x}_u \\ \boldsymbol{w}\, t_w + \boldsymbol{x}_w &= \boldsymbol{v}\, t_v + \boldsymbol{x}_v \end{aligned} \tag{13}$$

Hence:

$$\begin{pmatrix} t_w \\ t_u \\ t_v \end{pmatrix} = \begin{pmatrix} w_x & u_x & -v_x \\ w_y & u_y & -v_y \\ w_z & u_z & -v_z \end{pmatrix}^{-1} (\boldsymbol{x}_v - \boldsymbol{x}_u) \tag{14}$$

Therefore the positions $\boldsymbol{u}\, t_u + \boldsymbol{x}_u$ and $\boldsymbol{v}\, t_v + \boldsymbol{x}_v$ respectively on $\mathcal{D}_u$ and $\mathcal{D}_v$ corresponding to the minimum distance δ are identified. In addition δ reads:

$$\delta = \left\| \boldsymbol{u}\, t_u + \boldsymbol{x}_u - \boldsymbol{v}\, t_v - \boldsymbol{x}_v \right\| \tag{15}$$

One can show that all pairs of nonparallel dendrites families simultaneously reach their geometrical intersection in 2D or the minimum distance between them in 3D. Therefore, all conflicts are identified between all pairs of dendrites families by simple analytical geometrical calculations instead of time consuming incremental procedure. The FOG criterion is then applied both in 2D and 3D to determine which dendrite family continues to propagate while the other one is stopped.

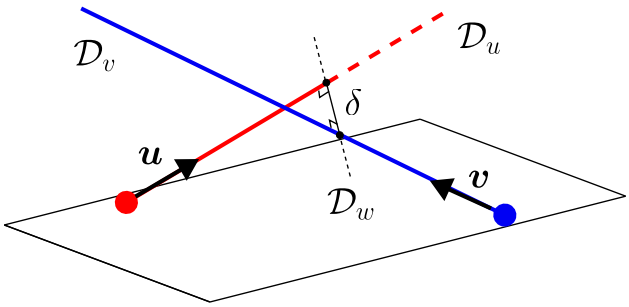

Figure 4: FOG criterion in 3D.

4) *Construction rule of Voronoi tessellations*. In the following, to efficiently implement 1), 2) and 3), Voronoi tessellations are used. The main advantage of using Voronoi tessellations is the small number of DoFs (i.e., seeds coordinates). Indeed, Voronoi tessellations are defined by N *seeds* denoted by $\boldsymbol{x}_j \in \mathbb{R}^3$ (where $1 \leq j \leq N$). Each cell denoted by C_j (where $1 \leq j \leq N$) is defined as follows:

$$C_j = \left\{ \boldsymbol{x} \in \mathbb{R}^3,\, \forall k \in \{1, \cdots, N\},\, \left\| \boldsymbol{x} - \boldsymbol{x}_j \right\|^2 \leq \left\| \boldsymbol{x} - \boldsymbol{x}_k \right\|^2 \right\} \tag{16}$$

Thus, the total number of DoFs is $3\,N$, while for CA techniques if N_{vox} denotes the number of voxels along one direction, the typical number of DoFs is N_{vox}^3, where usually $N < N_{\text{vox}}$. The proposed approach therefore holds considerable potential in reducing computation time.
Voronoi tessellations are constructed according to the following procedure. (i) Grains surrounding the melt are considered with their crystal orientation by introducing the corresponding seeds. In addition, in the region where equiaxed dendritic growth takes place randomly distributed seeds are created so that the average distance between seeds corresponds to the computed grain size (7), and random crystal orientations are affected to those seeds. (ii) Competitive epitaxial growth is considered from the grains in contact with the melt. To do so, a time discretization is introduced with a time step denoted by Δt. At each time step the ASF (i.e., the T_{ASF}-isotherm) is updated according to the temperature field history. Starting from an existing seed, a new one is added along the thermal gradient direction $\boldsymbol{d}_{\text{grain}}(\boldsymbol{x})$ (with $\boldsymbol{x} \in \Gamma_t(T_{\text{ASF}})$) according to (9). New seeds are added according to this procedure until the corresponding dendrite direction is stopped in a conflict with an other dendrite direction. Then each set of cells sharing the same crystal orientation is gathered into a single grain.
It should be noted that each grain is usually defined as a unique cell, while in this contribution grains are defined as sets of cells sharing the same crystal orientation. This enables to define complex grain structures with curved grains. Boundaries between cells of a single grain carry zero energy as there is no crystal disorientation. Therefore the previously developed fast model of grain growth due to annealing condition relying on Voronoi-Laguerre tessellations [20] can be directly applied as a post-processing of the present work.
The proposed procedure is illustrated in 2D in figure 5 for a simple cooling condition. As shown in figure 6, it should be noted that it remains the same for melt pools translating at a given speed.

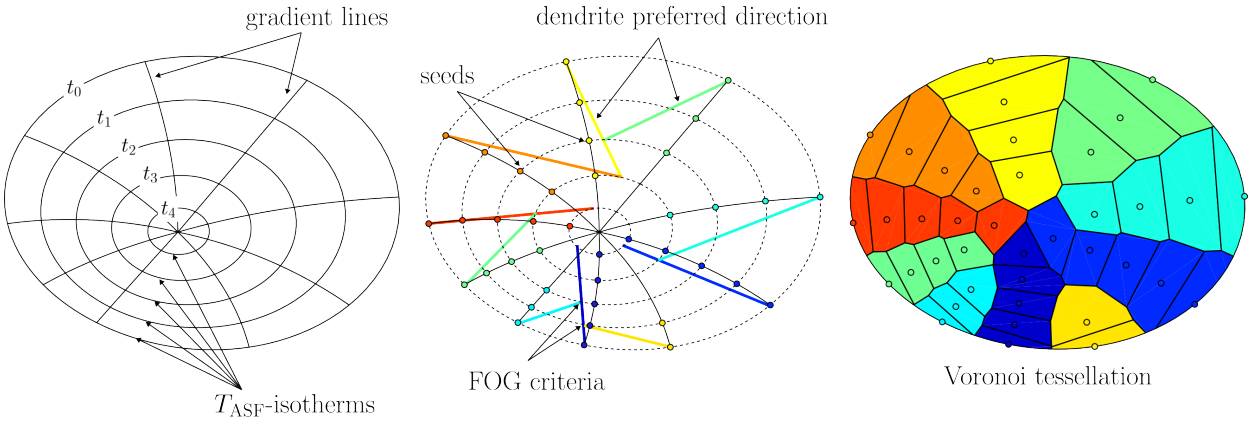

Figure 5: General principle for competitive columnar dendritic growth.

It should be emphasized that such an upscaling method can only capture the general behavior of melt pool solidification, and details associated to solutal and curvature undercooling are not taken into account, which does not able to consider anomalous dendritic growth for instance. The paper objectives though are limited to describe the average grain structure so that the morphological and crystallographic textures are correctly predicted within very short computation time.

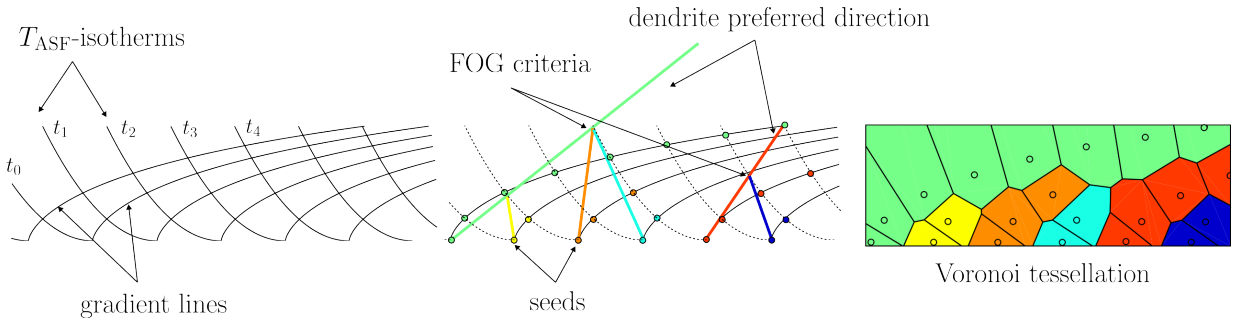

Figure 6: Principle for competitive columnar dendritic growth for melt pool translating at a given speed.

3. Results and discussion

The proposed approach has been implemented in *PYTHON* [34], which leads to a file containing the final Voronoi tessellation. Images are then produced with the free Voronoi-Laguerre tessellation software *NEPER* [35].

3.1. Comparison with experiments

In this section, the ability of the proposed strategy to capture the growth length of a grain before it is stopped in the competition with its neighbours is validated by comparison with well known experimental data [36]. A succinonitrile—1.3 wt% acetone transparent organic alloy behaving as metals is used, and a 2D columnar dendritic structure is obtained by trapping the melt between two glass sheets sufficiently closed to each other so that only one dendrite layer can grow. Thermal gradient is maintained vertical during grain solidification. Three grains are considered and crystal orientations are extracted from [36] hence the disorientation angles between thermal gradient and preferred growth directions, namely $\varphi_1 = 1°$, $\varphi_2 = 29.3°$ and $\varphi_3 = 5.5°$ (from the left to the right) are obtained and set in the numerical simulation. The comparison between the experiment and the numerical result is presented in figure 7. The growth length of the central grain is perfectly estimated by the proposed numerical strategy (see the red line in figure 7), even though plane orientations of GBs are not well captured so that the central grain is not triangular as in the experiment but rather in a channel shape. As already mentioned Voronoi tessellations do not enable to control GBs. Indeed, in this example seeds are arranged along 3 vertical lines (i.e., thermal gradient direction) corresponding to the 3 different grains, which induces the channel shape[1].

This comparison validates the main feature of the proposed numerical strategy, namely the ability to correctly capture when grain growth is stopped in the competition with neighboring grains. Nevertheless, the lack of control of GBs could appear as a significant drawback of the method as a large part of the literature focuses on GBs orientation. But as already mentioned, the present work is not aimed at studying in details a few grains but rather focus on large aggregates in which the lack of control of GBs is mitigated by geometric constraints between all grains so that the complete microstructure is satisfyingly captured. This is demonstrated in the following by comparing to the present work to PF and CA computations for 2D polycrystals.

[1]It should be noted that GBs are defined in Voronoi tessellations as the straight lines crossing perpendicularly the midpoint of the straight lines defined by adjacent pairs of seeds.

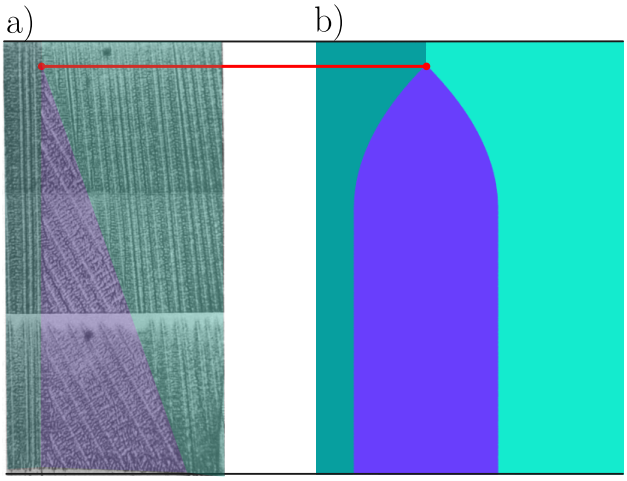

Figure 7: a) Experimental result [36]. The picture is extracted from [13] and modified with semi-transparent colors. b) Numerical results considering the same grains orientations. Both images have the same scale in order to compare the grain size.

3.2. Comparison with phase field and cellular automaton

In this section a comparison between PF, CA and the present model is provided in 2D. Simulation conditions and the corresponding PF and CA computations are extracted from [37]. A total of 15 simulations are analyzed, divided into 3 conditions named: "reference", "wide and shallow" and "deep and narrow" each of which contains 5 random draws of initial grain distribution. For each condition, the initial grain distribution is partially remelted according to the temperature field history given in analytical form in [37]. As detailed in section 2, the present work involves the computation of the ASF temperature denoted by $T_{\mathrm{ASF}}(t)$, which relies on the growth velocity (2) defined as a single power law. However, the growth velocity defined in [37] is written in the form of a sum a two power laws:

$$V(\boldsymbol{x},t) = \alpha_1\,\Delta T(\boldsymbol{x},t)^{\beta_1} + \alpha_2\,\Delta T(\boldsymbol{x},t)^{\beta_2} \tag{17}$$

Where $\alpha_1 = 6.45 \times 10^{-8}$, $\beta_1 = 3.83$, $\alpha_2 = 5.71 \times 10^{-6}$ and $\beta_2 = 1.98$. Therefore the best fitting power law (2) is identified and $\alpha = 1.16 \times 10^{-8}$ and $\beta = 3.08$. At each time step T_{ASF} is computed according to section 2, and presented in figure 8. It is clear that T_{ASF} very rapidly reaches the solidus temperature T_{sol} for all tested conditions (considering that complete solidification is reached in 0.00255 s). The T_{ASF}-isotherms are presented at different times in figure 9.

Voronoi tessellations are obtained as outputs of the present model. The PF and CA simulations, on the other hand, respectively involve 10 nm and 30 nm grids. However, all results are rasterized upon a 30 nm grid to facilitate comparisons. For each of the 3 tested conditions (i.e., "reference", "wide and shallow", and "deep and narrow") results are respectively presented in figures 10, 11, and 12 for the 1st of the 5 random draws of initial grain distributions. Very satisfying qualitative agreement is observed between the present work and CA, while more discrepancies can be observed with PF.

A more quantitative comparison is also provided by computing the Pearson correlation coefficient (PCC) between CA and the present work. To avoid overestimating the quality of the present

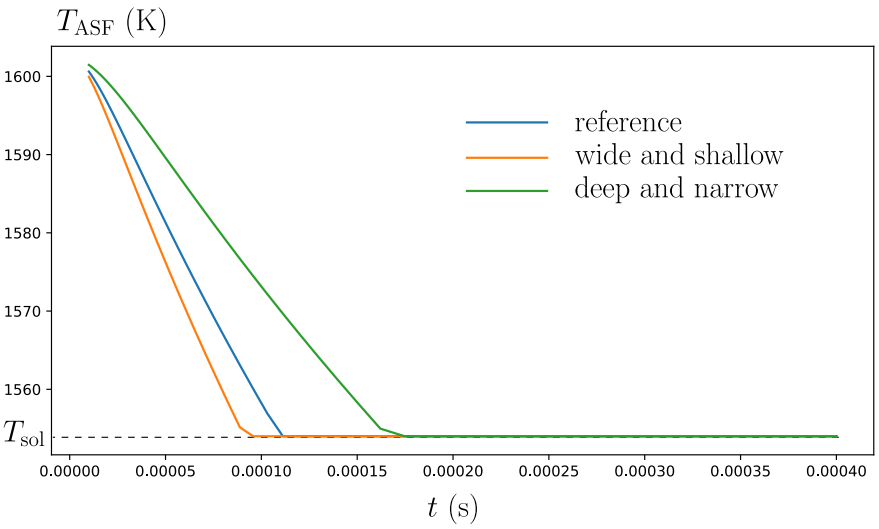

Figure 8: Evolution of T_{ASF} as a function of time for "reference", "wide and shallow" and "deep and narrow" conditions.

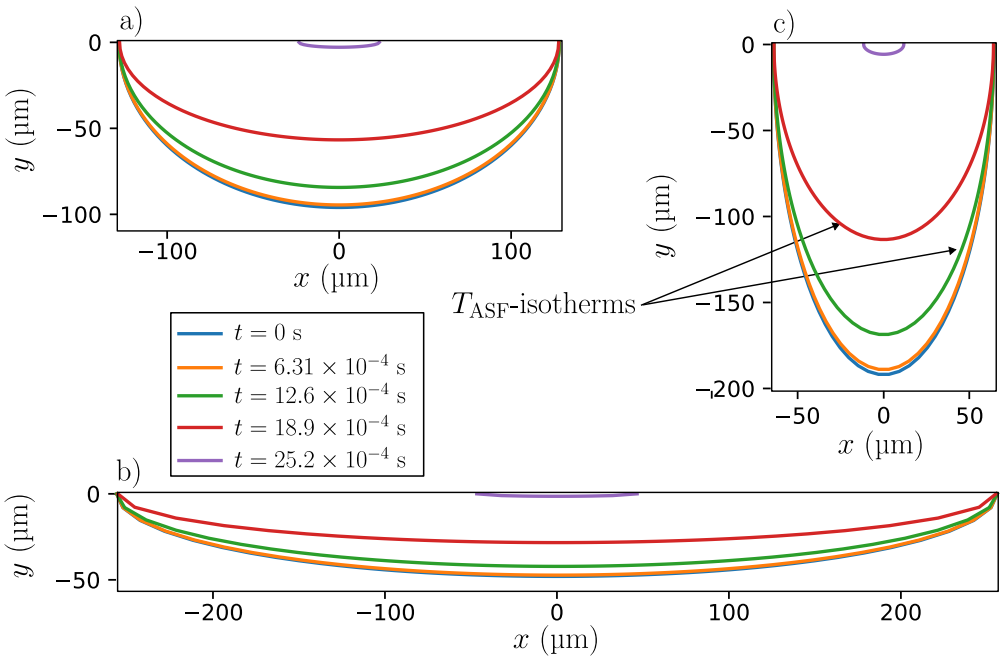

Figure 9: T_{ASF}-isotherms at different times for a) the "reference" condition, b) the "wide and shallow" condition and c) the "deep and narrow" condition.

work, PCCs were computed only in the remelted areas, i.e. excluding shaded areas in figures 10, 12 and 11 which are identical for all models. Results for the 15 tested simulations are listed in table 1. The present work correlates well with CA (i.e., PCCs around 0.7 in average). This demonstrates the ability of the present approach to capture the final grain structure after rapid solidification with similar results as finely discretized CA.

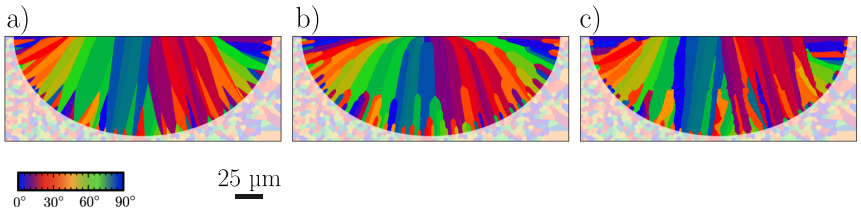

Figure 10: Results for one initial state of the "reference" condition obtained with a) CA, b) present work, and c) PF.

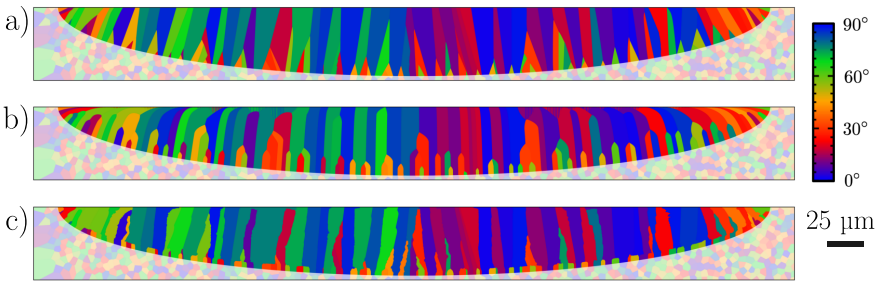

Figure 11: Results for one initial state of the "wide and shallow" condition obtained with a) CA, b) present work, and c) PF.

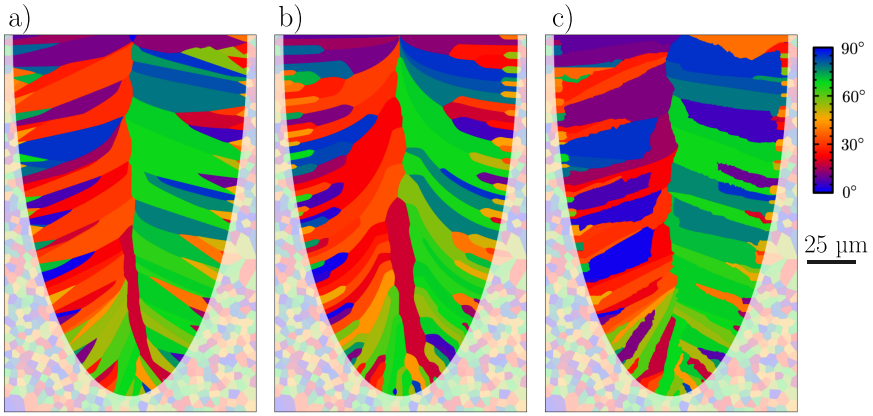

Figure 12: Results for one initial state of the "deep and narrow" condition obtained with a) CA, b) present work, and c) PF.

Table 1: PCC between all pairs of models for "reference" condition.

	1	2	3	4	5
Reference	0.804	0.800	0.780	0.710	0.679
Wide and shallow	0.735	0.719	0.759	0.793	0.694
Deep and narrow	0.728	0.691	0.662	0.696	0.620

In addition, computer vision techniques implemented in the *PYTHON* library *scikit-image* [38] are used to complement this analysis. For each grain an equivalent ellipse is defined by matching

the normalized second central moment of the grain. On this basis, statistical distributions of morphological and crystallographic textures are analyzed and compared between PF, CA and the present work. In figure 13 the statistical distribution of grain orientation (i.e., angle between the major axis and the horizontal direction) is presented. A good agreement is observed between the different models. In addition, one can notice that as expected grains are over-represented for inclinations close to the thermal gradient direction (i.e., around 90° for the "wide and shallow", 0°/180° for the "deep and narrow", while being more distributed around 90° for the "reference" condition). This is due to the favorable epitaxial growth along the thermal gradient direction. In figure 14, the statistical distribution of crystal orientations is presented. Once again a good agreement is observed between the different models. One can notice that crystal orientations close to the thermal gradient direction orientation are over-represented, which is due to competitive growth as only the grains whose crystal orientation is best aligned with the thermal gradient direction survive.

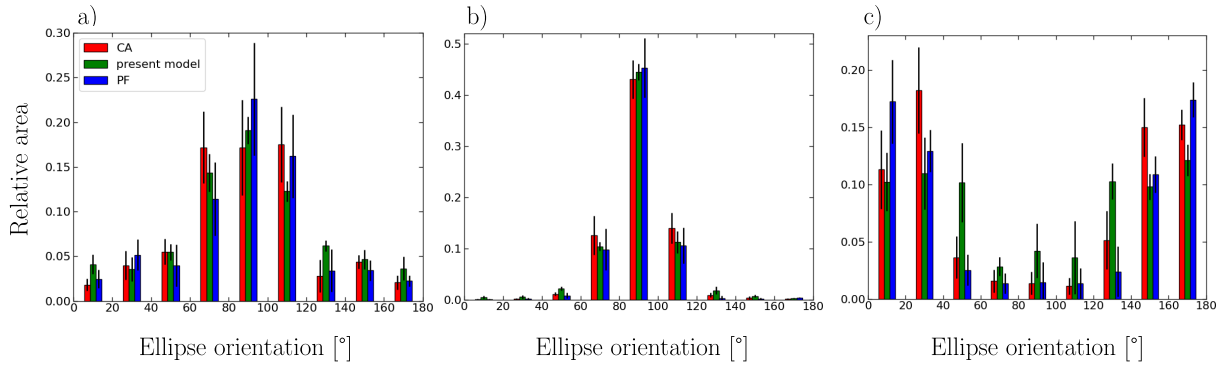

Figure 13: Distribution of grain orientation (i.e., the angle between the major axis and the horizontal direction) for: a) "reference" b) "wide and shallow" and c) "deep and narrow"

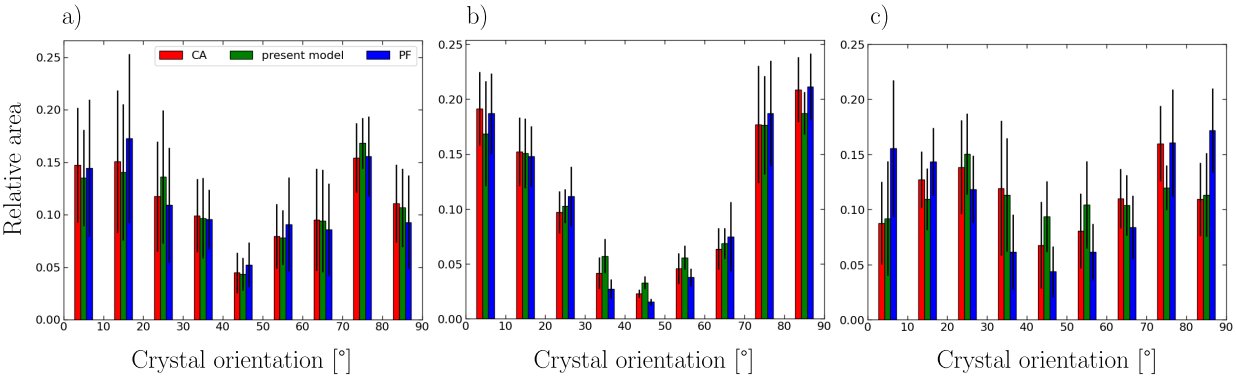

Figure 14: Distribution of of crystal orientations for: a) "reference" b) "wide and shallow" and c) "deep and narrow"

The computation cost reported in [37] is over 40 hours with highly parallelized implementation for PF computations. CA computations have been performed on a simple personal computer and

the computation cost is around 4 h for the finest grid size tested in [37]. In comparison, only a few seconds are necessary for the present work with a conventional laptop. This shows the computational cost reduction potential of the present work, which can be further improved by using a compiled programming language as *C++* instead of *PYTHON*.

3.3. Convergence analysis

Since a time discretization is introduced, a convergence analysis is provided in 3D. The simulation domain is defined by $(x, y, z) \in (0, L) \times (0, W) \times (0, H)$ where length, width and height are denoted by $L = 1$ mm, $W = 0.3$ mm, and $H = 0.377$ mm respectively, and where Cartesian coordinates are denoted by x, y, z. We consider a melt pool for which T_{ASF}-isotherm is moving on a substrate along the x direction at the constant speed $V_{\mathrm{melt}} = 10$ mm.s^{-1}. The melt pool shape (i.e., the T_{ASF}-isotherm) is set to a quarter of an ellipsoid, which reads:

$$\mathcal{M} = \left\{ (x, y, z) \in \mathbb{R}^3,\ \frac{x^2}{a^2} + \frac{y^2}{b^2} + \frac{z^2}{c^2} = 1,\ x \leq 0,\ z \leq 0 \right\} \tag{18}$$

Where a, b and c are the half-lengths of the axis defining the ellipsoid. The exact same substrate is used for all simulations as it plays the role of initial/boundary conditions for the growth competition between columnar dendritic grains. It is composed of randomly distributed equiaxed grains whose mean size is set to $d_0 = 0.01$ mm with random crystal orientations. The conflict detection threshold introduced in section 2 is set to $\delta_0 = 0.01$ mm. Parameters are summarized in table 2.

Table 2: Parameters for the convergence analysis.

Domain length	L	(mm)	1
Domain width	W	(mm)	0.3
Domain height	H	(mm)	0.377
Half-length axis	a	(mm)	2
Half-length axis	b	(mm)	0.2
Half-length axis	c	(mm)	0.387
Conflict detection threshold	δ_0	(mm)	0.01
Equiaxed grain size	d_0	(mm)	0.01
Melt pool velocity	V_{melt}	(mm.s^{-1})	10

A qualitative analysis of longitudinal sections and cross sections for different time discretization denoted by Δt is proposed. As shown in figure 15, two longitudinal sections are set at 50% and 55% of the width (i.e., respectively $y = 0.15$ mm and $y = 0.135$ mm) and one cross section is set at 50% (i.e., $x = 0.5$ mm). Since a steady state is considered (i.e., the melt pool moves at constant speed) the ASF velocity V_{ASF} is constrained by the melt pool velocity such as:

$$V_{\mathrm{ASF}}(\boldsymbol{x}, t) = V_{\mathrm{melt}}(\boldsymbol{x}, t) \cos(\theta(\boldsymbol{x}, t)) \tag{19}$$

Where θ is the angle between the grain growth direction $\boldsymbol{d}_{\mathrm{grain}}$ and the direction of movement of the melt pool $\boldsymbol{d}_{\mathrm{melt}}$ which is the horizontal direction in this case, which reads:

$$\theta(\boldsymbol{x}, t) = \arccos(\boldsymbol{d}_{\mathrm{melt}}(\boldsymbol{x}, t).\boldsymbol{d}_{\mathrm{grain}}(\boldsymbol{x}, t)) \tag{20}$$

Therefore, according to the proposed strategy detailed in section 2, the distance between two successive seeds denoted by $\delta_{\text{seed}} = V_{\text{ASF}}\,\Delta t$ reads:

$$\delta_{\text{seed}}(\boldsymbol{x}, t) = V_{\text{melt}}(\boldsymbol{x}, t)\cos(\theta(\boldsymbol{x}, t))\,\Delta t \tag{21}$$

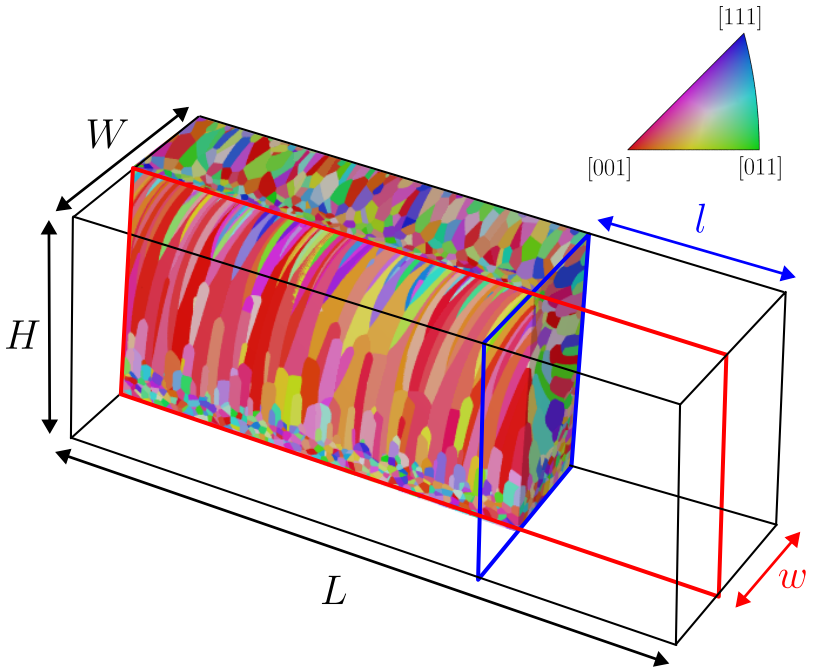

Figure 15: Selected cross sections from the 3D microstructure. Grain colors correspond to crystal orientations according to the vertical direction z.

Microstructures are presented for 8 different time steps Δt_i (with $1 \leq i \leq 8$) arranged in decreasing order, for the longitudinal sections in figures 16 and 17 and for the cross section in figure 18. Qualitatively, numerical simulations clearly seem to converge when the time step Δt decreases. This qualitative remark is completed by a quantitative convergence analysis. To do so, the following relative distance is used:

$$\xi = \frac{\|\boldsymbol{I}(\Delta t_i) - \boldsymbol{I}(\Delta t_8)\|}{\|\boldsymbol{I}(\Delta t_8)\|} \tag{22}$$

Where each image is a set of pixels gathered into vectors denoted by $\boldsymbol{I}(\Delta t_i)$ (with $1 \leq i \leq 8$). The relative error ξ is presented in log scale for longitudinal and cross sections in figure 19. The convergence rate is in Δt. Of course, this convergence analysis does not prove that the proposed strategy converges toward a solution that is representative of experimental results, but this aspect has already been broached in 2D in section 3.2, and should be extended in 3D in future works.

Qualitative comments of these numerical results should also be added. The obtained microstructures are similar to what is commonly observed in metal additive manufacturing, which

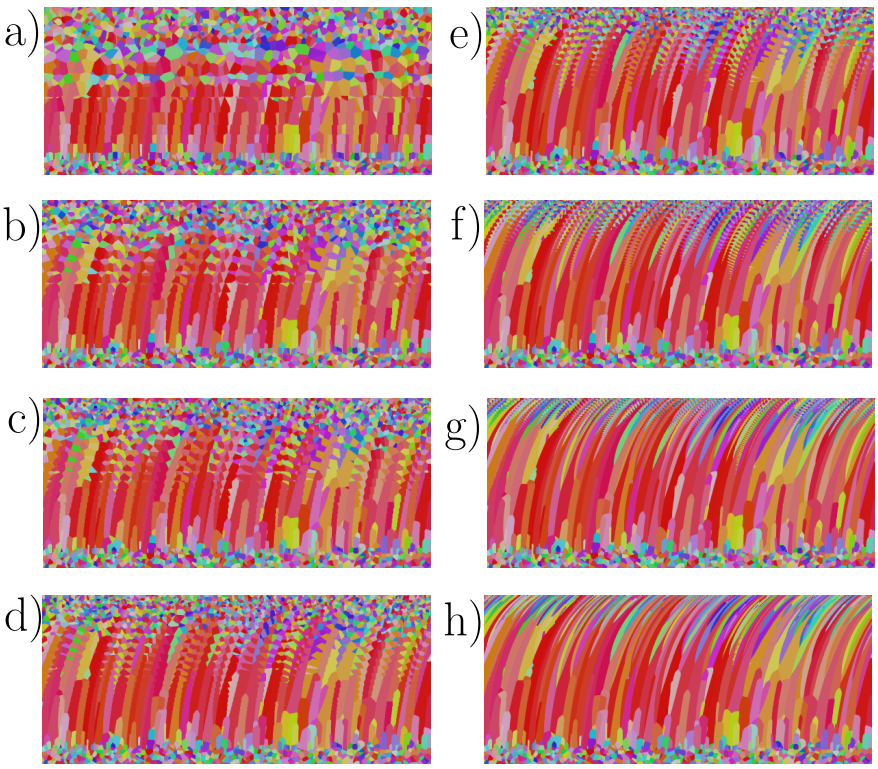

Figure 16: Longitudinal section at 50% of the width for a) $\Delta t_1 = 0.02$ s, b) $\Delta t_2 = 0.01$ s, c) $\Delta t_3 = 0.008$ s, d) $\Delta t_4 = 0.006$ s, e) $\Delta t_5 = 0.004$ s, f) $\Delta t_6 = 0.002$ s, g) $\Delta t_7 = 0.001$ s, and h) $\Delta t_8 = 0.0005$ s.

relies on moving melt pools as in the studied example. Indeed as reported in [39], for the longitudinal section at 50% (i.e., mid plane), the competitive growth mechanisms lead to microstructures characterized by elongated grains aligned with the vertical direction, and by the <100> crystal direction also aligned with the vertical direction. In addition, similar pattern as reported in [39] are obtained for the cross section. It is interesting to notice that the longitudinal section at 55% is significantly different from the longitudinal section at 50%, as the 3D microstructure rapidly evolves along the width direction. This highlights the benefits of the proposed fast numerical approach, which enables to rapidly estimate 3D microstructures, while experimental results obtained by electron backscatter diffraction techniques are often limited to single longitudinal and/or cross sections.

4. Conclusion

This paper presents an original and very fast numerical strategy to compute entire microstructures during melt pool solidification including the growth competition between columnar dendritic grains. The key contribution is twofold, 1) an upscaling approach is derived to obtain an average solidification front instead of detailing each dendrite individually, and 2) Voronoi tessellations are used instead of regular grids for numerical implementation so that the number of degrees of freedom is dramatically reduced in comparison to classical phase field or cellular automaton approaches (especially for three-dimensional microstructures). Numerical results have been compared to a

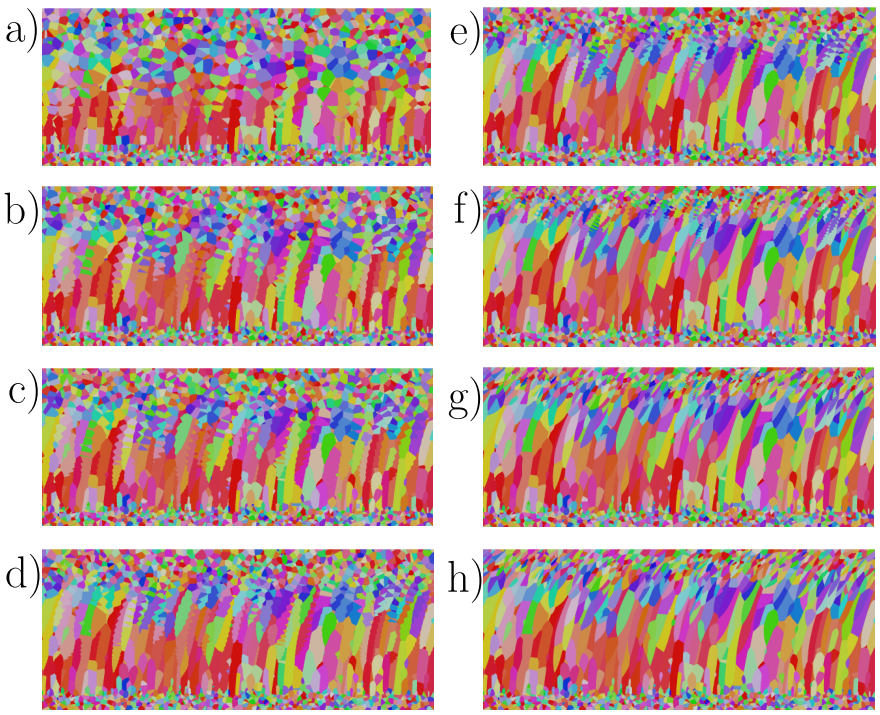

Figure 17: Longitudinal section at 55% of the width for a) $\Delta t_1 = 0.02$ s, b) $\Delta t_2 = 0.01$ s, c) $\Delta t_3 = 0.008$ s, d) $\Delta t_4 = 0.006$ s, e) $\Delta t_5 = 0.004$ s, f) $\Delta t_6 = 0.002$ s, g) $\Delta t_7 = 0.001$ s, and h) $\Delta t_8 = 0.0005$ s.

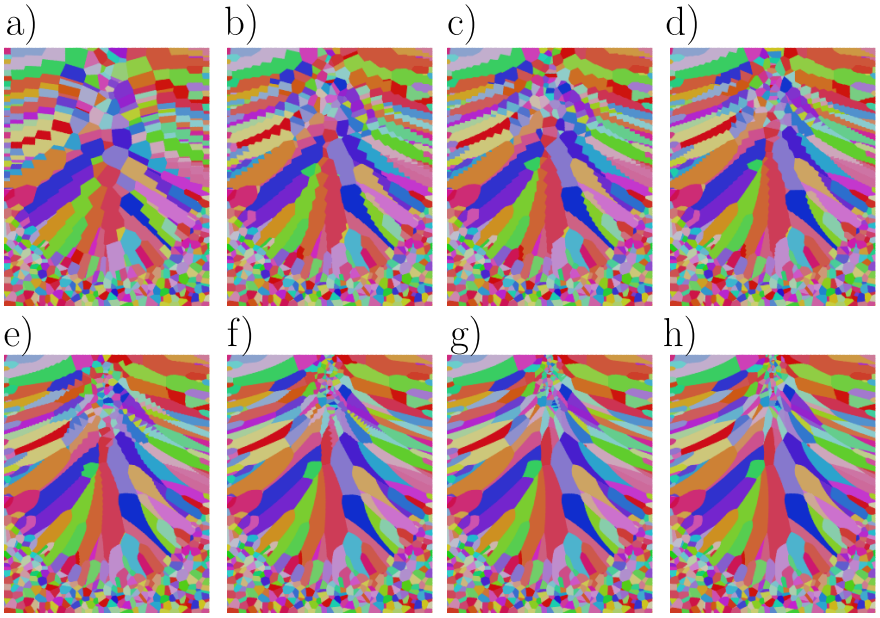

Figure 18: Cross section at 50% of the length for a) $\Delta t_1 = 0.02$ s, b) $\Delta t_2 = 0.01$ s, c) $\Delta t_3 = 0.008$ s, d) $\Delta t_4 = 0.006$ s, e) $\Delta t_5 = 0.004$ s, f) $\Delta t_6 = 0.002$ s, g) $\Delta t_7 = 0.001$ s, and h) $\Delta t_8 = 0.0005$ s.

classical experiment and excellent agreement is observed for the growth length during the competition with neighboring grains. Grain boundaries orientation though have been found to be incorrect,

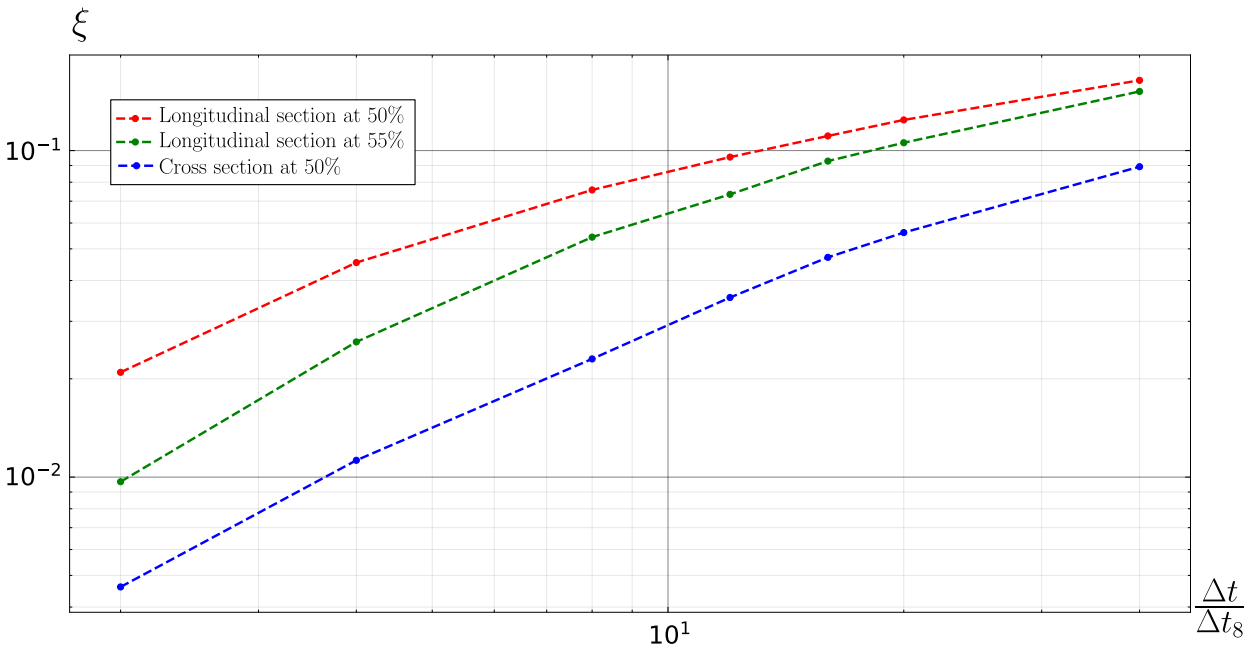

Figure 19: Convergence analysis for longitudinal sections and cross section.

which is due to the fact Voronoi tessellation do not enable to control grain boundaries. However, this effect is mitigated for large aggregates. Indeed, a detailed comparison with two-dimensional phase field and cellular automaton simulations give evidences that entire microstructures are satisfyingly captured. In addition, the proposed approach gives similar results as cellular automaton, while reducing computation time from more than 40 hours for PF and 4 hours for CA to a few seconds for the present work. Three-dimensional comparisons are left for future work to further validate the model. Computations in 3D involving a moving melt pool also showed interesting potential in predicting microstructures in metal additive manufacturing for instance.

This work holds considerable potential in computation cost reduction for 2D and 3D simulations of microstructures, which enables to carry out large numbers of simulations with different random draws of equiaxed grain nucleation from which epitaxial growth takes place. Statistical exploration of probability density function of morphological and crystallographic textures is therefore accessible. In addition, large data bases of numerical computations can be collected so that machine learning algorithms can be trained for real time control of solidification processes.

Acknowledgement

The authors are very grateful to Damien Tourret (IMDEA Materials Institute) for his availability and for sharing numerical data containing phase field and cellular automaton computations, which enabled to compare and validate the present work.

Funding. : This work was supported by the french national research agency (ANR) for project MIFASOL.

Authors contribution. : Q.D contributed to model development, code programming and writing. D.W.P contributed to model development, writing, supervision and fund acquisition.

Data availability statement. : Data will be made available on requiest.

References

[1] J. A. Dantzig, M. Rappaz, Solidification: -Revised & Expanded, EPFL press, 2016.

[2] S. Kou, Welding metallurgy, New Jersey, USA (2003) 431–446.

[3] L. Nastac, J. Valencia, M. Tims, F. Dax, Advances in the solidification of in718 and rs5 alloys, Superalloys 718 (2001) 625–706.

[4] A. Limare, S. Popinet, C. Josserand, Z. Xue, A. Ghigo, A hybrid level-set/embedded boundary method applied to solidification-melt problems, Journal of Computational Physics 474 (2023) 111829.

[5] N. Moelans, B. Blanpain, P. Wollants, An introduction to phase-field modeling of microstructure evolution, Calphad 32 (2008) 268–294.

[6] W. J. Boettinger, J. A. Warren, C. Beckermann, A. Karma, Phase-field simulation of solidification, Annual review of materials research 32 (2002) 163–194.

[7] A. Pineau, G. Guillemot, D. Tourret, A. Karma, C.-A. Gandin, Growth competition between columnar dendritic grains – cellular automaton versus phase field modeling, Acta Materialia 155 (2018) 286–301.

[8] J. Li, Z. Wang, Y. Wang, J. Wang, Phase-field study of competitive dendritic growth of converging grains during directional solidification, Acta Materialia 60 (2012) 1478–1493.

[9] D. Tourret, A. Karma, Multiscale dendritic needle network model of alloy solidification, Acta materialia 61 (2013) 6474–6491.

[10] D. Tourret, A. Karma, Three-dimensional dendritic needle network model for alloy solidification, Acta Materialia 120 (2016) 240–254.

[11] P.-A. Geslin, C.-H. Chen, A. M. Tabrizi, A. Karma, Dendritic needle network modeling of the columnar-to-equiaxed transition. part i: two dimensional formulation and comparison with theory, Acta Materialia 202 (2021) 42–54.

[12] C.-H. Chen, A. M. Tabrizi, P.-A. Geslin, A. Karma, Dendritic needle network modeling of the columnar-to-equiaxed transition. part ii: three dimensional formulation, implementation and comparison with experiments, Acta Materialia 202 (2021) 463–477.

[13] C.-A. Gandin, M. Rappaz, A coupled finite element-cellular automaton model for the prediction of dendritic grain structures in solidification processes, Acta metallurgica et materialia 42 (1994) 2233–2246.

[14] T. Carozzani, H. Digonnet, C.-A. Gandin, 3d cafe modeling of grain structures: application to primary dendritic and secondary eutectic solidification, Modelling and Simulation in Materials Science and Engineering 20 (2011) 015010.

[15] K. Teferra, D. J. Rowenhorst, Optimizing the cellular automata finite element model for additive manufacturing to simulate large microstructures, Acta Materialia 213 (2021) 116930.

[16] J. Li, M. Sage, X. Guan, M. Brochu, Y. F. Zhao, Machine learning-enabled competitive grain growth behavior study in directed energy deposition fabricated ti6al4v, Jom 72 (2020) 458–464.

[17] M. Rappaz, C.-A. Gandin, Probabilistic modelling of microstructure formation in solidification processes, Acta metallurgica et materialia 41 (1993) 345–360.

[18] M. Rolchigo, S. T. Reeve, B. Stump, G. L. Knapp, J. Coleman, A. Plotkowski, J. Belak, Exaca: A performance portable exascale cellular automata application for alloy solidification modeling, Computational Materials Science 214 (2022) 111692.

[19] D. Weisz-Patrault, S. Sakout, A. Ehrlacher, Fast simulation of grain growth based on Orientated Tessellation Updating Method, Mechanics & Industry 21 (2020) 513.

[20] S. Sakout, D. Weisz-Patrault, A. Ehrlacher, Energetic upscaling strategy for grain growth. I: Fast mesoscopic model based on dissipation, Acta Materialia 196 (2020) 261–279.

[21] D. Weisz-Patrault, S. Sakout, A. Ehrlacher, Energetic upscaling strategy for grain growth. II: Probabilistic macroscopic model identified by Bayesian techniques, Acta Materialia (2021).

[22] D. Walton, B. Chalmers, The origin of the preferred orientation in the columnar zone of ingots, Trans. Metall. Soc. AIME 215 (1959).
[23] H. Wang, X. Zhang, J. Meng, J. Yang, Y. Yang, Y. Zhou, X. Sun, A new model of competitive grain growth dominated by the solute field of the nickel-based superalloys during directional solidification, Journal of Alloys and Compounds 873 (2021) 159794.
[24] T. Takaki, M. Ohno, Y. Shibuta, S. Sakane, T. Shimokawabe, T. Aoki, Two-dimensional phase-field study of competitive grain growth during directional solidification of polycrystalline binary alloy, Journal of Crystal Growth 442 (2016) 14–24.
[25] H. Yu, J. Li, X. Lin, L. Wang, W. Huang, Anomalous overgrowth of converging dendrites during directional solidification, Journal of crystal growth 402 (2014) 210–214.
[26] S. Paul, J. Liu, S. T. Strayer, Y. Zhao, S. Sridar, M. A. Klecka, W. Xiong, A. C. To, A discrete dendrite dynamics model for epitaxial columnar grain growth in metal additive manufacturing with application to inconel, Additive Manufacturing 36 (2020) 101611.
[27] G. L. Knapp, N. Raghavan, A. Plotkowski, T. Debroy, Experiments and simulations on solidification microstructure for inconel 718 in powder bed fusion electron beam additive manufacturing, Additive Manufacturing 25 (2019) 511–521.
[28] A. Prasad, L. Yuan, P. Lee, M. Patel, D. Qiu, M. Easton, D. StJohn, Towards understanding grain nucleation under additive manufacturing solidification conditions, Acta Materialia 195 (2020) 392–403.
[29] M. C. Flemings, Solidification processing, Metallurgical and Materials Transactions B 5 (1974) 2121–2134.
[30] A. Edwards, D. Weisz-Patrault, E. Charkaluk, Analysis and fast modelling of microstructures in duplex stainless steel formed by directed energy deposition additive manufacturing, Additive Manufacturing 61 (2023) 103300.
[31] S. Chen, Three dimensional Cellular Automaton–Finite Element (CAFE) modeling for the grain structures development in Gas Tungsten/Metal Arc Welding processes, Ph.D. thesis, Ecole Nationale Supérieure des Mines de Paris, 2014.
[32] J. Deschamps, M. Georgelin, A. Pocheau, Growth directions of microstructures in directional solidification of crystalline materials, Physical Review E 78 (2008) 011605.
[33] D. Walton, B. Chalmers, The origin of the preferred orientation in the columnar zone of ingots, Transactions of the American Institute of Mining and Metallurgical Engineers 215 (1959) 447–457.
[34] G. Van Rossum, F. L. Drake Jr, Python reference manual, Centrum voor Wiskunde en Informatica Amsterdam, 1995.
[35] R. Quey, P. Dawson, F. Barbe, Large-scale 3d random polycrystals for the finite element method: Generation, meshing and remeshing, Computer Methods in Applied Mechanics and Engineering 200 (2011) 1729–1745.
[36] H. Esaka, W. Kurz, Columnar dendrite growth: experiments on tip growth, Journal of crystal growth 72 (1985) 578–584.
[37] S. Elahi, R. Tavakoli, I. Romero, D. Tourret, Grain growth competition during melt pool solidification—comparing phase-field and cellular automaton models, Computational Materials Science 216 (2023) 111882.
[38] S. Van der Walt, J. L. Schönberger, J. Nunez-Iglesias, F. Boulogne, J. D. Warner, N. Yager, E. Gouillart, T. Yu, scikit-image: image processing in python, PeerJ 2 (2014) e453.
[39] C. Guévenoux, S. Hallais, A. Charles, E. Charkaluk, A. Constantinescu, Influence of interlayer dwell time on the microstructure of inconel 718 laser cladded components, Optics & Laser Technology 128 (2020) 106218.